electronics

Article

Quantitative Analysis of Steel Alloy Elements Based on LIBS and Deep Learning of Multi-Perspective Features

Yanhong Gu [1], Zhiwei Chen [1], Hao Chen [2] and Fudong Nian [1,3,*]

[1] Institute of Advanced Manufacturing Engineering, Hefei University, Hefei 230601, China; guyh@hfuu.edu.cn (Y.G.); chenzhiwei667@gmail.com (Z.C.)
[2] School of Mechanical Engineering, Suzhou University of Science and Technology, Suzhou 215009, China; hchen@mail.usts.edu.cn
[3] Anhui Provincial Engineering Technology Research Center of Intelligent Vehicle Control and Integrated Design Technology, Hefei 230601, China
* Correspondence: nianfudong@outlook.com

Abstract: The Si and Mn contents in steel alloys are important characteristic indexes that influence the plasticity and welding properties of these alloys. In this work, the quantitative analysis methods for trace elements under complex alloy matrices by laser-induced breakdown spectroscopy (LIBS) are studied, which provide a foundation for utilizing LIBS technology in the rapid online detection of steel alloy properties. To improve the quantitative analysis accuracy of LIBS, deep learning algorithm methods are introduced. Given the characteristics of LIBS spectra, we explore multi-perspective feature extraction and backward differential methods to extract the spatio-temporal characteristics of LIBS spectra. The Text Convolutional Neural Network (TextCNN) model, combined with multi-perspective feature extraction, displays good stability and lower average relative errors (6.988% for Si, 6.280% for Mn) in the test set compared to the traditional quantitative analysis method and deep neural network (DNN) model. Finally, the backward differential method is employed to optimize the two-dimensional LIBS spectral input matrix, and the results indicate that the average relative errors of Si and Mn elements in the test set decrease to 5.139% and 3.939%, respectively. The method proposed in this work establishes a theoretical basis and technical support for precise prediction and online quality monitoring.

Keywords: laser-induced breakdown spectroscopy (LIBS); convolutional neural networks; multi-perspective feature; backward difference; steel alloys; quantitative analysis

Citation: Gu, Y.; Chen, Z.; Chen, H.; Nian, F. Quantitative Analysis of Steel Alloy Elements Based on LIBS and Deep Learning of Multi-Perspective Features. *Electronics* **2023**, *12*, 2566. https://doi.org/10.3390/electronics12122566

Academic Editor: Maciej Ławryńczuk

Received: 10 May 2023
Revised: 29 May 2023
Accepted: 1 June 2023
Published: 6 June 2023

1. Introduction

Metallic inclusions, such as silicon (Si) and manganese (Mn), have an immediate impact on the hardness, plasticity, and strength of steel alloys [1,2]. When Si content is below 0.6% (wt) and Mn content is below 1.5% (wt), the hardness and strength of steel alloys significantly improve. However, as Si and Mn contents increase, the plasticity, toughness, and welding properties of steel alloys gradually weaken, affecting the quality of steel alloys [3,4]. Laser-induced breakdown spectroscopy (LIBS) has become a promising elemental online detection technique for industrial applications owing to its attributes of real-time, rapid, multi-component simultaneous detection, and low requirement of sample preparation [5,6]. However, due to the complex elemental compositions of steel alloys, LIBS technology outputs complex spectral data containing peak overlaps and interference between characteristic spectral lines [7,8]. How to effectively extract available characteristic information from complicated high-dimensional spectral data and improve the precision of quantitative analysis has become the focus of research [9,10].

In recent years, deep learning methods have become a focus in quantitative analysis research for LIBS due to their powerful self-learning ability and sharp senses of discovering the intrinsic patterns in high-dimensional data [11,12]. Convolutional neural network

(CNN) is a typical deep learning algorithm which extracts useful information and reduces high dimensionality. Numerous researchers have focused on the research of LIBS by CNN [13]. Pengfei Zhang et al. [14] used a Resnet network to quantify the elemental compositions from LIBS signals on Mars, which effectively reduced the prediction error of measuring elements. Yun Zhao et al. [15] applied LIBS and principal component analysis (PCA) combined with deep learning networks to classify tobacco soil samples and calculate the composition of Pb in soils. Xuebin Xu et al. [16] used CNN to detect the concentrationa of N, P, and K in soil samples by LIBS and the relative errors of prediction decreased to 7.5%. Pengju Xing et al. [17] applied LIBS and DP-CNN to detect Li in seawater, and the mean squared error of prediction was close to 3.48%.

The quantitative analysis of steel alloys using LIBS is hindered by two problems: peak overlaps and interference, as well as the high dimensionality of data. In order to overcome these problems, this paper proposes a methodology, which employs TextCNN combined with a multi-perspective feature extraction method to extract features from the distribution information of the spectral data and reduce dimensionality. Following that, the backward differential method was used to optimize the input variables for TextCNN. The proposed method was applied to analyze the trace elements Si and Mn in steel alloys accurately.

2. Experiments

2.1. LIBS Instrumentation

The experimental setup for LIBS is depicted in Figure 1. As shown in Figure 1, the instrument was equipped with an Nd:YAG laser (λ = 1064 nm), working at 90 mJ per pulse in about 10 ns, at a repetition rate of 10 Hz with the corresponding laser fluence of 230 J/cm^2. The laser beam was focused on the surface of a steel alloy pellet perpendicularly via a 10 cm focal length lens. To ensure accuracy, the sample was placed on a two-dimensional rotary platform, which stabilizes the repeated measurements. The plasma radiation was collected by a set of 38.1 mm focal length lenses and coupled into a mid-step grating spectrometer (Andor Mechelle 5000, Andor Technology, London, England). The spectrometer covers a wide range of wavelengths from 220 nm to 850 nm with a spectral resolution of 0.1 nm, providing 23,399 channels for each spectrum. An ICCD detector (Andor, DH734i-18F-03) was used to detect the signal.

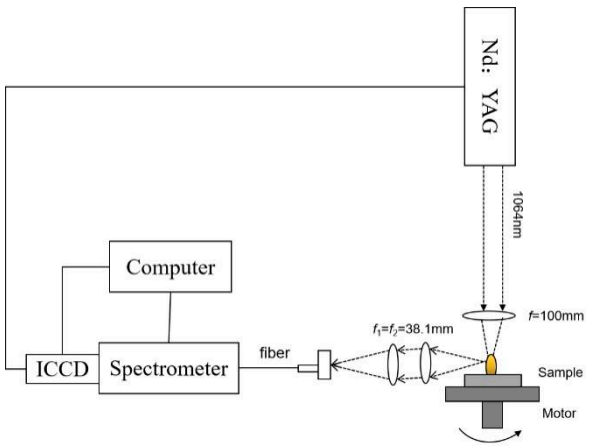

Figure 1. Schematic diagram of the LIBS experiment set-up.

2.2. Steel Alloy Samples

Thirteen steel alloy samples labeled 1# to 13# were provided and certified by the German Federal Institute for Materials Testing (BAM). Prior to all the experimentation, all the surfaces of the steel alloy samples were smoothed by sandpapers. The main trace elements contained in the samples were Si, Mn, C, Cr, Ni, and Mo., and the elemental contents are listed in Table 1.

Table 1. The contents of elements in steel alloys (%).

Sample	Si	Mn	C	Cr	Ni	Mo
1#	0.460	0.740	0.092	12.350	12.550	—
2#	0.374	0.686	0.0103	14.724	6.124	0.0138
3#	0.463	0.722	0.0345	11.888	12.850	0.0304
4#	0.270	1.400	0.0190	18.460	10.200	0.2650
5#	0.570	0.791	0.0860	25.390	20.05	—
6#	0.405	1.380	0.0660	17.310	9.24	0.0920
7#	0.480	1.311	0.0141	17.840	10.20	—
8#	1.410	1.700	0.1430	17.960	8.90	—
9#	0.210	0.890	0.0500	14.140	5.66	1.590
10#	0.537	1.745	0.0201	16.811	10.720	2.1110
11#	0.531	1.016	0.0489	14.630	24.680	—
12#	0.344	0.897	0.0223	18.370	12.330	—
13#	0.344	0.897	0.0223	18.370	12.330	—

2.3. Data Acquisition and Preprocessing

In order to determine the optimal delay time and gate width, repetition tests were carried out. The signal-background-ratio (SBR) values of Fe I:425.075 nm were calculated. The relationship between the SBR values and delay times is shown in Figure 2. As a result, the SBR initially increases and then decreases with the increase of detection delay. Considering the effects of detection delay and gate width on the intensity of laser plasma, the final optimal delay time and gate width for the subsequent experiments can be set as 1.5 μs and 2 μs, respectively. To reduce the inhomogeneity of the samples, 10 spectra were acquired from each sample and each spectrum was accumulated with 60 laser pulses. Overall, a total of 130 spectra were collected from 13 steel alloy samples. To improve the stability of the spectra, all measured spectral data were normalized using the maximum value.

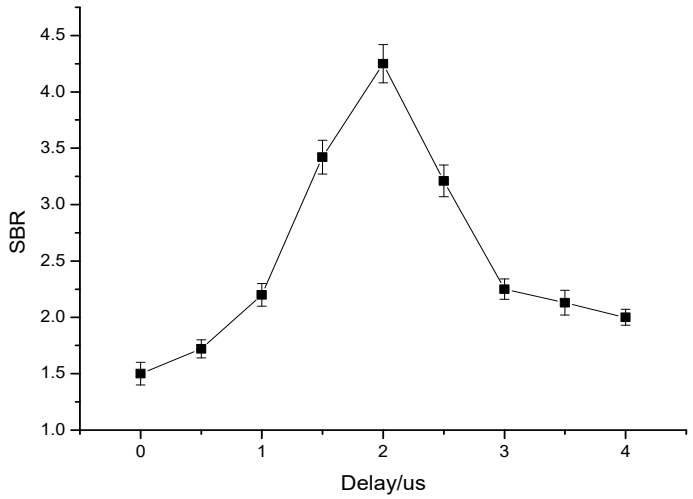

Figure 2. The dependent of SBR for the element of Si on different detection delay.

3. Results and Discussion

3.1. Traditional Calibration Method

Figure 3 illustrates the calibration curves of Si and Mn by traditional quantitative analysis method. Herein, the characteristic spectral lines of Si and Mn in steel alloys were identified through NIST database, and Si I: 288.158 nm and Mn I:403.076 nm were selected. As can be seen from Figure 3, the linear correlation coefficient for Si is 0.68, while the linear correlation coefficient for Mn is lower than 0.33.

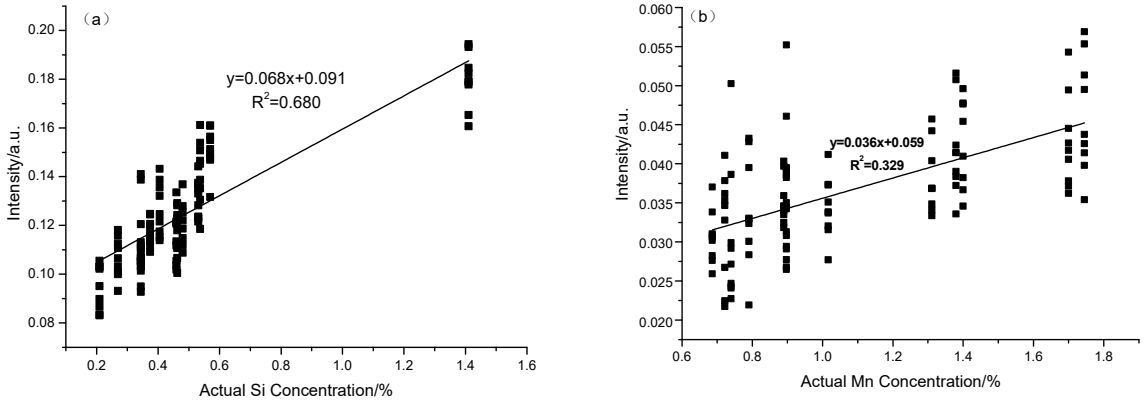

Figure 3. Calibration curve with a traditional quantitative method. (**a**) Si; (**b**) Mn.

Figure 4 displays a typical LIBS spectrum of a steel alloy sample. The LIBS spectrum shows various emission lines and clearly indicates that there are serious peak overlaps and inference between the characteristic spectral lines of the analytic elements and the matrix element Fe. Moreover, the spectral line intensity of Mn I:403.076 nm is weak, and the other three spectral lines of Mn (Mn I:403.307 nm, Mn I:403.449 nm, Mn I:403.573 nm) are closely situated, exacerbating the problems of peak overlaps and interference. Therefore, the traditional quantitative analysis method was deemed inadequate for determining the elements Si and Mn in steel alloys with complicated matrices.

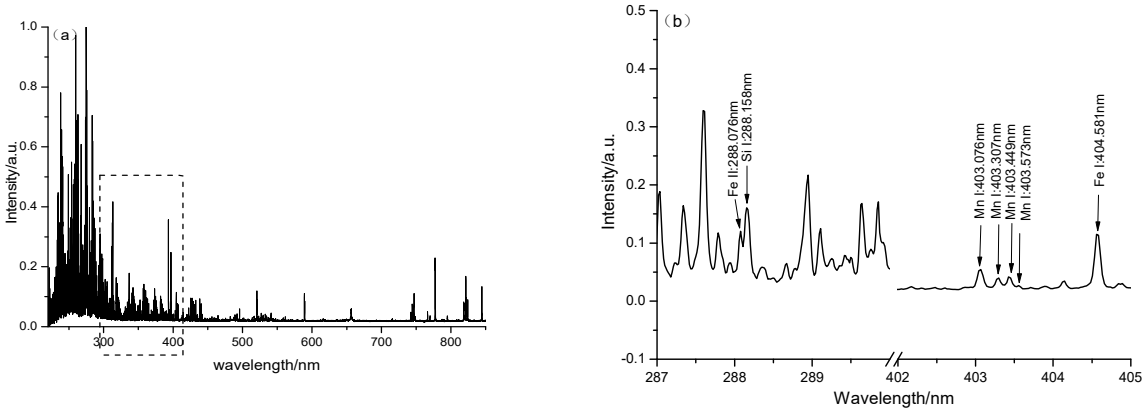

Figure 4. A typical LIBS spectrum of the steel sample; (**a**) 220–850 nm; (**b**) 287–405 nm.

Figure 5 illustrates the calibration curves of Si and Mn by multivariate linear regression method. Herein, the characteristic spectral lines of Si are Si I:250.690 nm, Si I:252.411 nm, Si I: 288.158 nm, Si II:413.090 nm, and Fe I:404.581 nm. The characteristic spectral lines of Mn are Mn I:403.076 nm, Mn I:403.307 nm, Mn I:403.449 nm, Mn I:403.573 nm, and Fe I:404.581 nm. As can be seen from Figure 5, the linear correlation coefficient for Si is 0.797 and the linear correlation coefficient for Mn is only 0.702. The accuracy of the fitting curves is still insufficient.

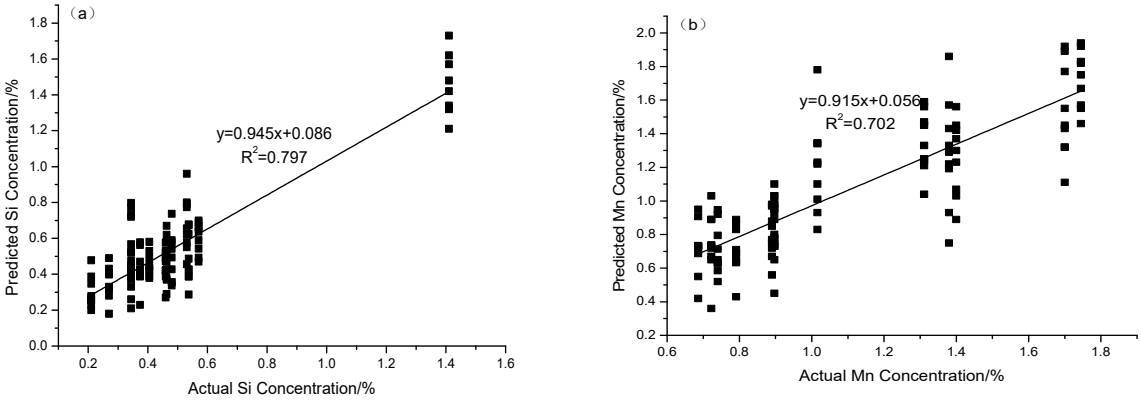

Figure 5. Calibration curve with multivariate linear regression method. (**a**) Si; (**b**) Mn.

Deep learning algorithms are potential methods which deeply mine the implied information and filter out irrelevant data from spectral data to improve the quantitative accuracy. The deep learning algorithms used in this paper were written by Matlab 2019a, and the Adam optimizer was used to optimize the model parameters. The initial learning rate was set to 0.00001, and a total of 1000 training iterations (epoch) were conducted. The measured spectral data were divided into a training set and a test set, with the first nine measurements of each sample assigned to the training set and the tenth measurement assigned to the test set.

3.2. Deep Neural Networks (DNN)

DNN is a network architecture that consists of at least two hidden layers, and all layers of the network are fully connected. In this work, we employed a four-hidden-layer feedback neural network with a Leaky ReLU activation function and linear units combined with leak correction for the fitting model. The structural diagram of DNN used in this paper is presented in Figure 6. As shown in Figure 6, the DNN has 23,399 input variables and two output variables (the contents of the two analytic elements). The hidden layers comprise 2048, 1024, 512, and 256 neurons, respectively. To alleviate the issue of overfitting, a dropout layer was incorporated after the last fully connected layer. The output layer contains two output vectors, y_1 represents the predicted content of Si, and y_2 represents the predicted content of Mn.

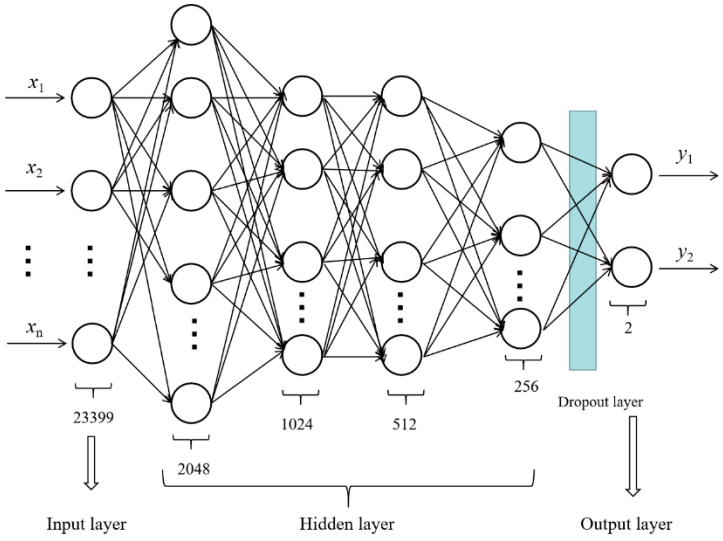

Figure 6. Structural diagram of DNN model.

Figure 7 shows the calibration and prediction results by the DNN model. The correlation coefficient values are 0.996 for both Si and Mn, while the average relative standard deviations for the training set are 2.181% and 1.515% for Si and Mn, respectively. Table 2 reports the prediction results of Si and Mn in the test set based on the trained DNN model, and the average relative errors are 10.086% and 10.324% for Si and Mn, respectively. The results of the quantitative analysis indicate that although the DNN model performed well in the calibration set, the results in the test set suggest that the model cannot precisely predict the concentrations of Si and Mn. Therefore, to improve the accuracy of prediction, a more advanced deep learning algorithm should be imported to consider more characteristics of the LIBS spectra.

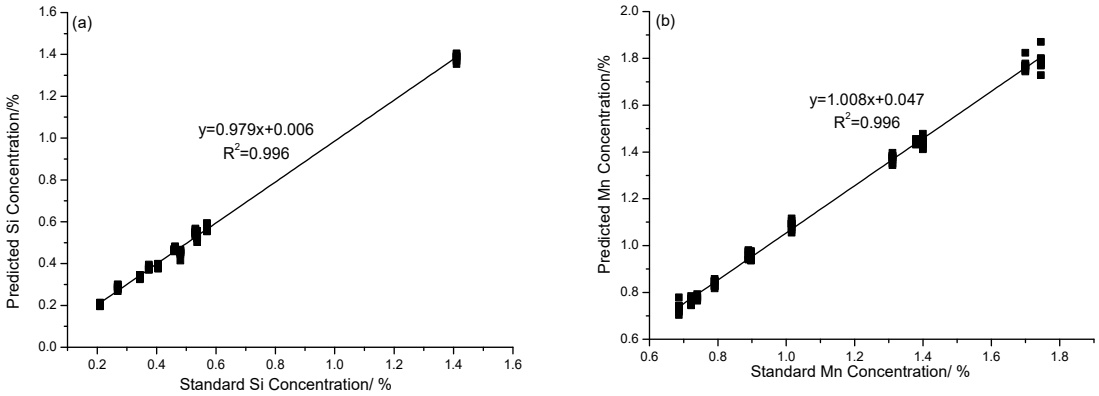

Figure 7. Calibration curve with DNN model for the training set. (**a**) Si; (**b**) Mn.

Table 2. Test set results by DNN model.

Si			Mn		
Actual Concentration/%	**Predicted Concentration/%**	**Relative Error/%**	**Actual Concentration/%**	**Predicted Concentration/%**	**Relative Error/%**
0.460	0.436	5.217	0.740	0.814	10.000
0.374	0.385	2.941	0.686	0.934	36.152
0.463	0.448	3.24	0.722	0.802	11.080
0.270	0.321	18.899	1.400	1.374	1.857
0.570	0.626	9.825	0.791	0.994	25.664
0.405	0.396	2.222	1.380	1.277	7.464
0.480	0.370	22.917	1.311	1.329	1.373
1.410	0.900	36.17	1.700	1.432	15.765
0.210	0.230	9.524	0.890	1.023	14.944
0.537	0.592	10.242	1.745	1.596	8.539
0.531	0.520	2.072	1.016	1.01	0.591
0.344	0.368	6.977	0.897	0.9	0.334
0.344	0.341	0.872	0.897	0.901	0.450

3.3. TextCNN

The severe peak overlaps and interference in LIBS spectra are evident in Figure 4. To alleviate the impact of problems for quantitative analysis, TextCNN uses convolutional kernels as intermediaries to achieve partial connection of upper- and lower-layer neurons, actualizing the characteristic digging and filtering via sliding windows for high-precision quantitative prediction of elemental contents in steel alloys. The structural diagram of TextCNN used in this study is illustrated in Figure 8. To meet the input layer requirements of TextCNN, a multi-perspective feature extraction method was used to construct a two-dimensional LIBS spectral data matrix with 256 convolutional kernels of sizes of 5 × 1 and step sizes of 3. Each convolutional kernel can be regarded as a filter to extract the features of the original one-dimensional LIBS spectral data from different perspectives, generating

a column vector of size of 2601 × 1. Arrange these 256 column vectors in sequential horizontal order, forming a matrix of size 2601 × 256. This matrix was transposed and used as the input layer. Then TextCNN uses multiple convolutional kernels with different structure sizes (2 × 2601, 3 × 2601, 4 × 2601, 5 × 2601, 6 × 2601, 7 × 2601, 8 × 2601, 9 × 2601, and 256 each) to extract local features of the LIBS spectral data and quantify elemental contents effectively. The activation function is a Leaky ReLU function with linear units combined with leak correction, and the pooling layer values are the maximum values of the convolution selected as the feature values. To alleviate the issue of overfitting, a dropout layer was incorporated after the last fully connected layer.

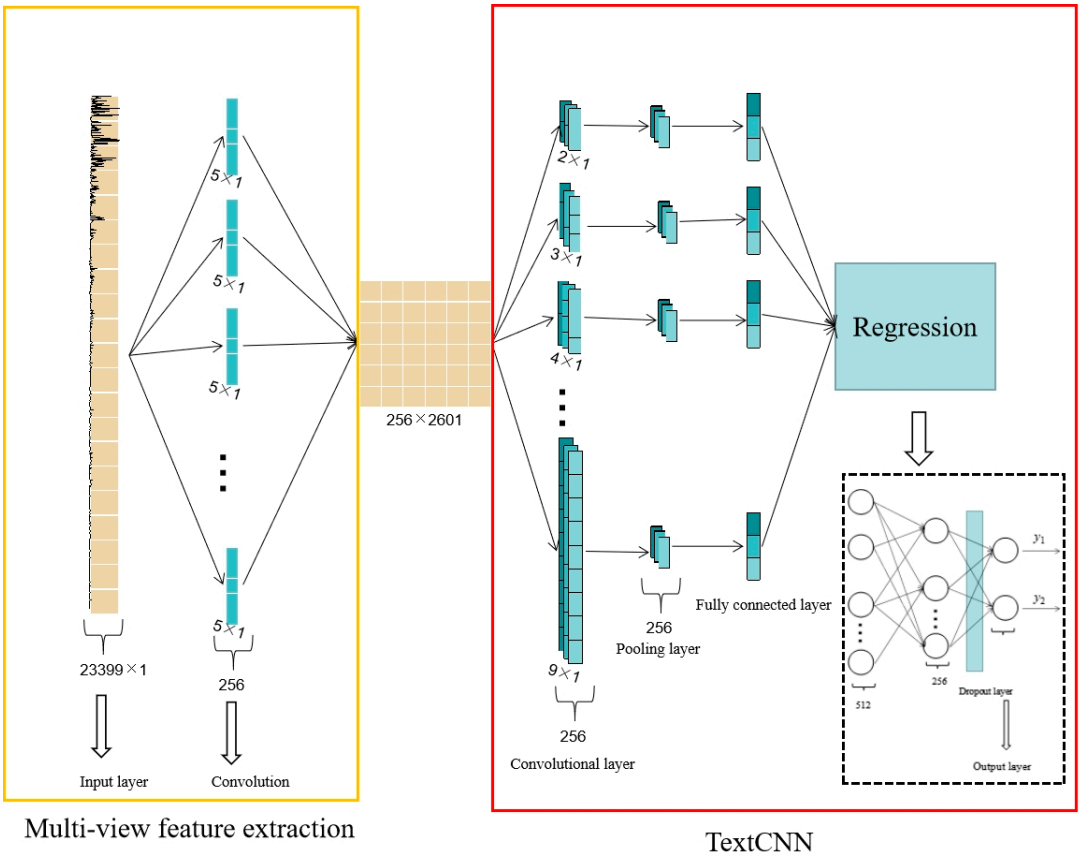

Figure 8. Structural diagram of TextCNN model.

Figure 9 shows the prediction relative errors and the storage sizes of the model by the TextCNN model with different convolutional kernels. The overall prediction relative errors are closer to 0 with 256 convolutional kernels, and the storage size of the model increases with the increase of convolutional kernels. This reflects that with the increase of the dimension, more parameters and a small amount of the data make it difficult to train the model. Considering the results of the prediction relative errors and the storage sizes of the model, the final convolutional kernels for the TextCNN model can be set to 256.

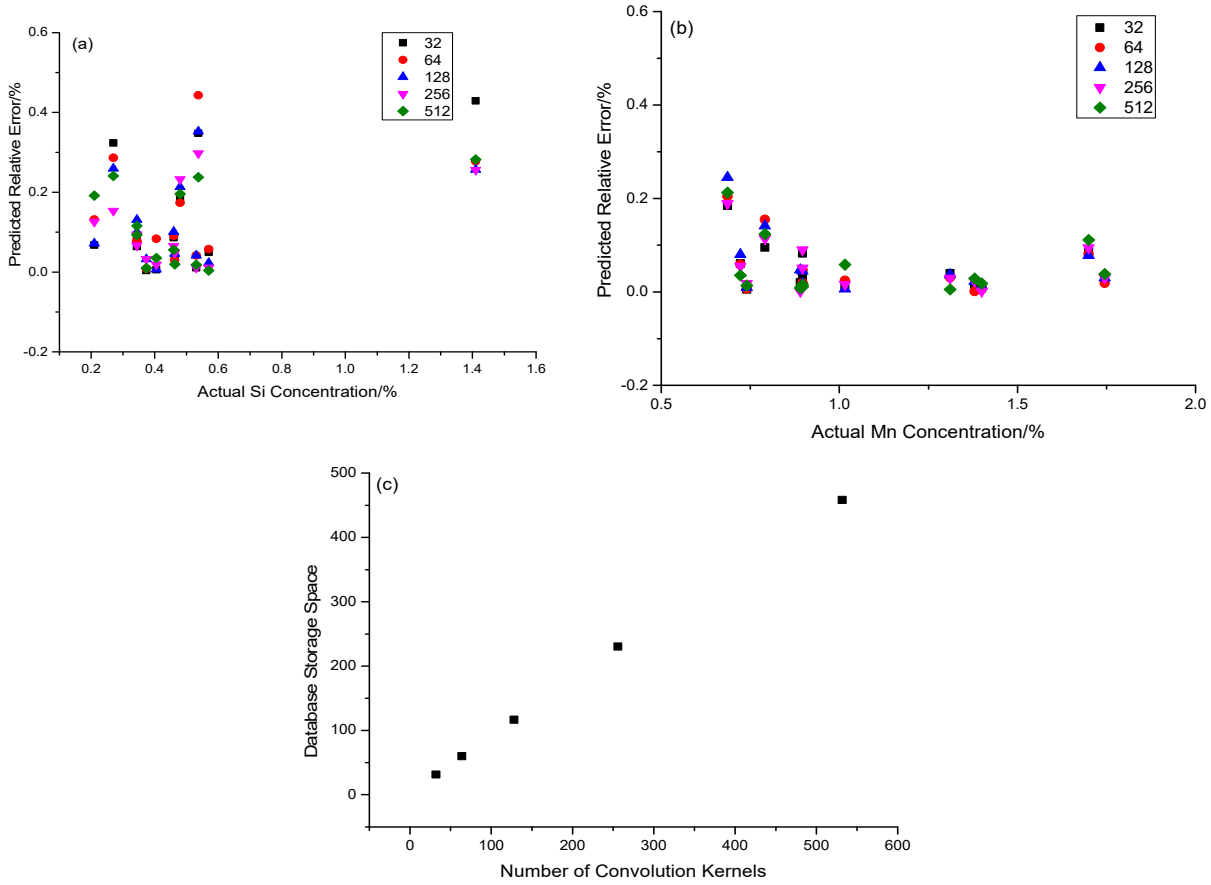

Figure 9. Prediction relative errors and the storage sizes of the model by TextCNN with different convolutional kernels. (**a**) Si; (**b**) Mn; (**c**) database stroage space.

Figure 10 illustrates the calibration and prediction results by the TextCNN model. The correlation coefficient values are 0.990 and 0.998 for Si and Mn, while the average relative standard deviations for the training set are 2.505% and 1.109% for Si and Mn, respectively. Table 3 reports the prediction results of Si and Mn in the test set based on the trained TextCNN model, and the average relative errors for the test set are decreased to 6.988% and 6.280% for Si and Mn, respectively. The result implies that the calibration accuracy for steel alloys can be improved by TextCNN. Perhaps TextCNN is effective at capturing local dependencies in data through the use of convolutional filters. These filters slide over the input data, capturing important local features and patterns. In contrast, traditional CNNs are mainly designed to capture spatial dependencies in data. However, it is worth noting that some test samples still exhibit poor precision in the relative error of the predictions, which may be attributed to the low concentrations of the measured elements in these samples.

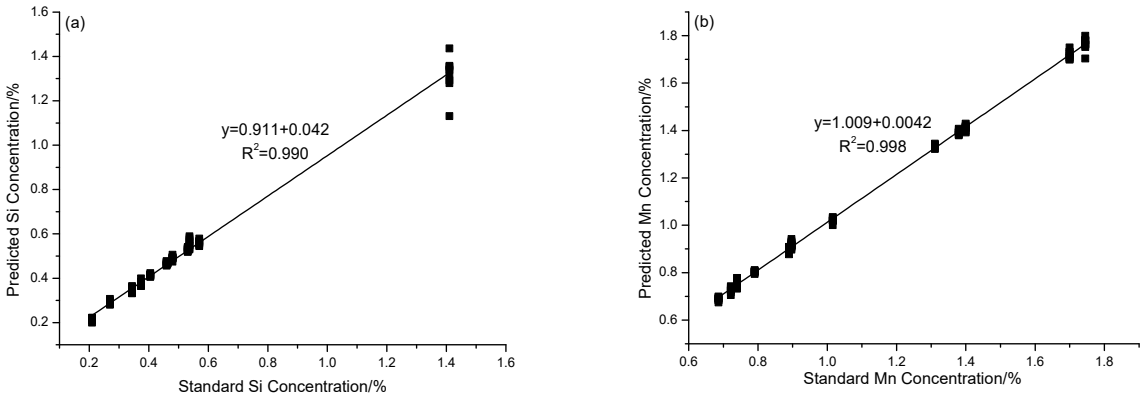

Figure 10. Calibration curve with the TextCNN model for the training set. (**a**) Si; (**b**) Mn.

Table 3. Test set results by TextCNN model.

Si			Mn		
Actual Concentration/%	**Predicted Concentration/%**	**Relative Error/%**	**Actual Concentration/%**	**Predicted Concentration/%**	**Relative Error/%**
0.460	0.433	5.87	0.740	0.758	2.432
0.374	0.406	8.556	0.686	0.844	23.032
0.463	0.45	2.808	0.722	0.731	1.247
0.270	0.306	13.333	1.400	1.338	4.429
0.570	0.618	8.421	0.791	0.909	14.918
0.405	0.416	2.716	1.380	1.275	7.609
0.480	0.411	14.375	1.311	1.299	0.915
1.410	1.272	9.787	1.700	1.498	11.882
0.210	0.229	9.048	0.890	0.866	2.697
0.537	0.603	12.291	1.745	1.609	7.794
0.531	0.538	1.318	1.016	0.999	1.673
0.344	0.344	0.000	0.897	0.888	1.003
0.344	0.352	2.326	0.897	0.879	2.007

3.4. Backward-Differential TextCNN

Figure 11 presents five characteristic spectra of the 10# steel alloy sample in the spectral range of 403–404 nm. As shown in Figure 11, the fine structures of the characteristic spectral lines of Mn, such as form, location, and width, differ noticeably, which significantly affects the training results of the quantitative model. To normalize the characteristic data of the LIBS spectra and improve the learning performance of the TextCNN model, the first-order backward difference method was used to process the one-dimensional spectral data. Two two-dimensional LIBS spectral data matrix were constructed by multi-perspective feature extraction method with 256 convolutional kernels of sizes of 5×1 and step sizes of 3. The original two-dimensional LIBS spectral data matrix are represented as X1 and the backward difference two-dimensional LIBS spectral data matrix are represented as X2. X1 is input to TextCNN1 and X2 is input to TextCNN2. Finally, the data processed by the two networks were fused and inputted to the fully connected layer. To alleviate the issue of overfitting, a dropout layer was incorporated after the last fully connected layer. The schematic structure of the backward-differential TextCNN model is shown in Figure 12.

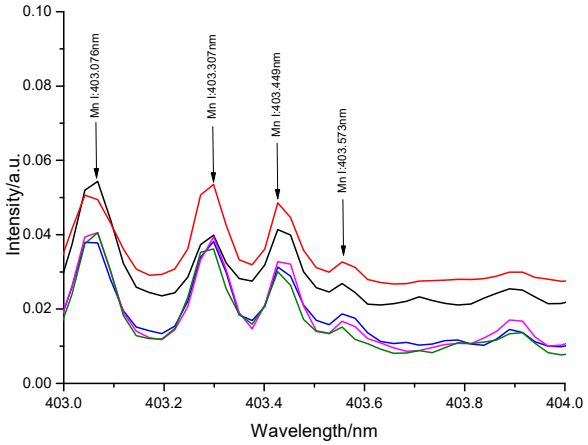

Figure 11. Five characteristic spectra of the 10# steel sample in the range of 403–404 nm.

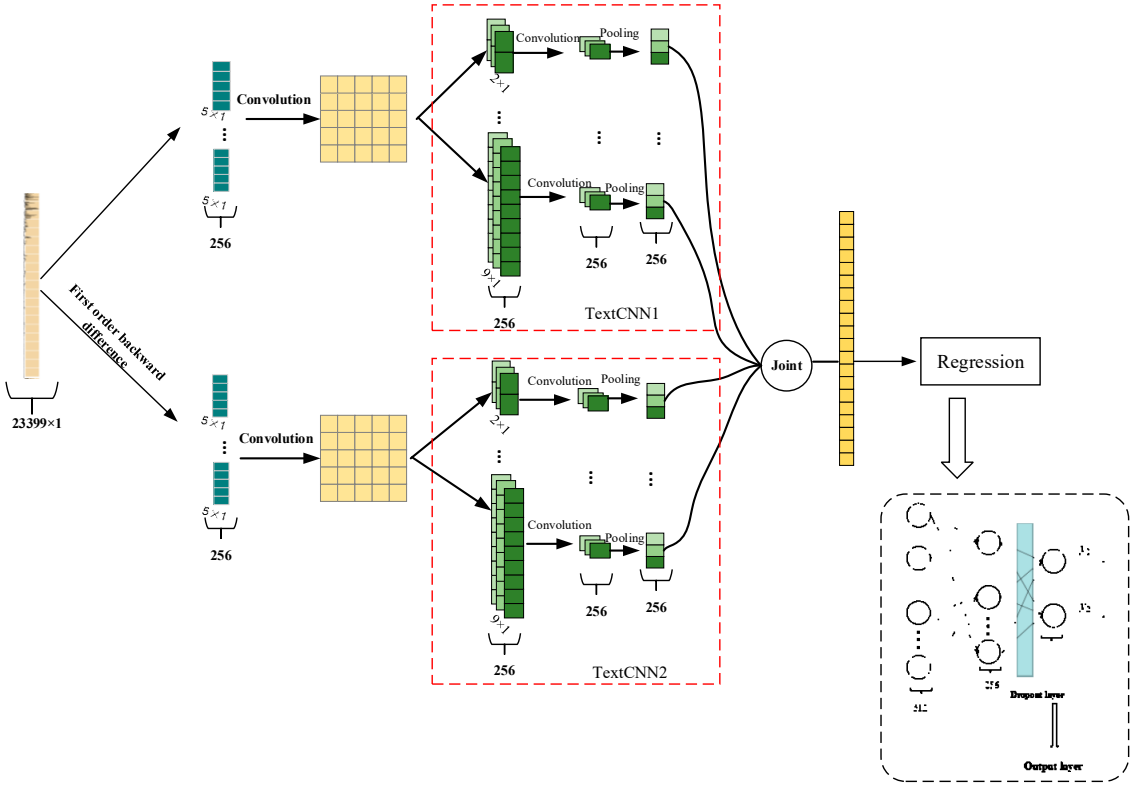

Figure 12. Structural diagram of the backward-differential TextCNN model.

Figure 13 shows the calibration and prediction results by the backward-differential TextCNN model. The correlation coefficient values are 0.997 and 0.993 for Si and Mn, while the average relative standard deviations for the training set are 2.397% and 1.664% for Si and Mn, respectively. Table 4 reports the prediction results of Si and Mn in the test set based on the trained backward-differential TextCNN model, and the average relative errors for the test set are decreased to 5.139% and 3.956% for Si and Mn, respectively. Importantly, all the relative errors of the predictions for the test samples are lower than 9.5%, indicating that the backward-differential TextCNN model has significant potential in the quantitative analysis of steel alloys.

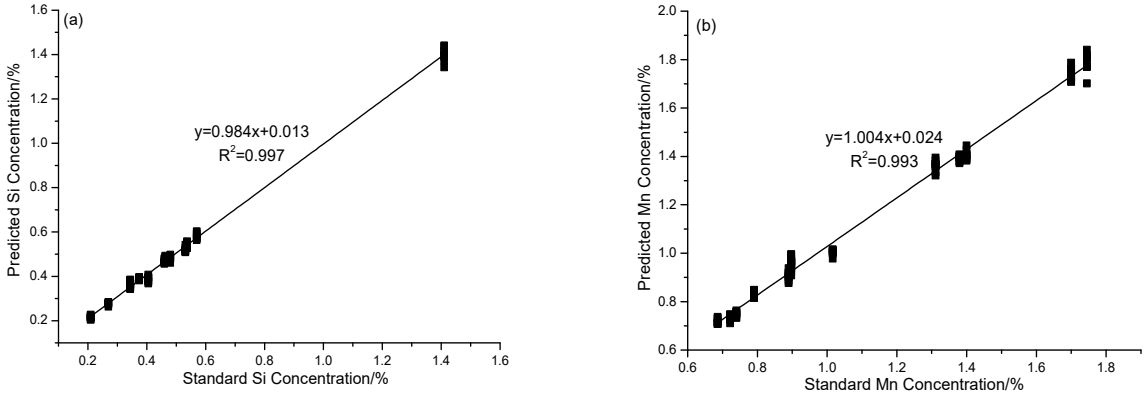

Figure 13. Calibration curve with the backward-differential TextCNN model for the training set. (**a**) Si; (**b**) Mn.

Table 4. Test set results by backward-differential TextCNN model.

Si			Mn		
Actual Concentration/%	**Predicted Concentration/%**	**Relative Error/%**	**Actual Concentration/%**	**Predicted Concentration/%**	**Relative Error/%**
0.460	0.430	6.522	0.740	0.753	1.757
0.374	0.362	3.209	0.686	0.715	4.227
0.463	0.441	4.752	0.722	0.762	5.540
0.270	0.291	7.778	1.400	1.398	0.143
0.570	0.576	1.053	0.791	0.841	6.321
0.405	0.397	1.975	1.380	1.348	2.319
0.480	0.449	6.458	1.311	1.350	2.975
1.410	1.350	4.255	1.700	1.540	9.412
0.210	0.227	8.095	0.890	0.890	0.000
0.537	0.567	5.587	1.745	1.692	3.037
0.531	0.537	1.13	1.016	1.032	1.575
0.344	0.312	9.302	0.897	0.851	5.128
0.344	0.321	6.686	0.897	0.816	9.030

In this study, we evaluated the deviation between the predicted contents by the trained quantitative analysis models and the actual contents of Si and Mn using the mean absolute error (MAE) as the loss function. The loss change curves of the three neural network models during the training progress are presented in Figure 14. As can be seen from Figure 14, the loss values gradually decrease and stabilize with the increase of training times for all three models. However, the backward-differential TextCNN model has lower loss values compared to the DNN and TextCNN models, indicating that it is better at predicting the actual contents. Table 5 shows the average predicted relative errors of Si and Mn for the test set by the three neural network models. The results in Figure 14 and Table 5 demonstrate that the backward-differential TextCNN model can effectively correct the differences in fine structures of the characteristic spectral lines, deeply exploit the multi-perspective characteristics of the spectral data, and filter out irrelevant information, which can favorably improve the forecasting accuracy.

Table 5. The average relative errors of the three neural network models for the test set.

DNN		TextCNN		Backward-Differential TextCNN	
Si	**Mn**	**Si**	**Mn**	**Si**	**Mn**
10.086	10.324	6.988	6.280	5.139	3.959

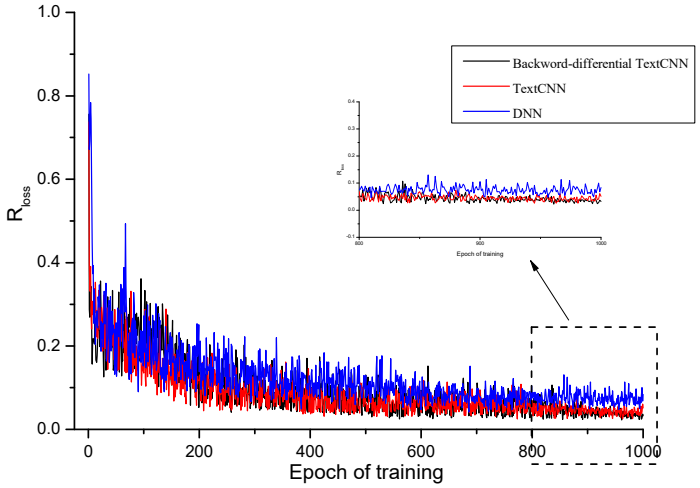

Figure 14. Comparison of R_{loss} in the regression training of the three neural network models.

4. Conclusions

In this paper, we proposed a novel LIBS quantitative analysis method that combines multi-perspective feature extraction and backward-differential method with TextCNN. The contents of Si and Mn in steel alloys were successfully determined by LIBS and the model. The correlation coefficients for Si and Mn are both above 0.993, which implies that the trained model can accurately predict unknown steel alloy samples. The results also demonstrate that the backward-differential TextCNN has lower predicted average relative errors for the test set (5.139% for Si and 3.939% for Mn) than DNN (10.086% for Si and 10.324% for Mn) and TextCNN (6.988% for Si and 6.280% for Mn). These results gained through this experiment prove that the proposed backward-differential TextCNN method provides a new approach for trace elemental quantitative analysis of complex samples with severe peak overlaps and interference, improving the forecasting accuracy by extracting the spatio-temporal characteristics of the LIBS spectra.

Author Contributions: Conceptualization, methodology, and writing—original draft preparation, Y.G.; writing—review and editing, H.C.; visualization, Z.C.; funding acquisition, F.N. All authors have read and agreed to the published version of the manuscript.

Funding: This work was supported by the Natural Science Foundation of Anhui Province (No. 2008085QF316), the Research Foundation of Education Bureau of Anhui Province (No. 2022AH051783), the Science and Technology Development Plan Foundation of Suzhou (No. SS202148), the China Postdoctoral Science Foundation (Nos. 2020M671383) and Anhui Provincial Key Research and Development Program (No. 2022a05020042).

Data Availability Statement: The code is publicly available at http://github.com/nianfd/QASAE.

Conflicts of Interest: There are no conflict of interest to declare.

References

1. Ali, S.; Rani, A.M.A.; Altaf, K.; Hussain, P.; Prakash, C.; Hastuty, S.; Na Rao, T.V.V.L.; Aliyu, A.A.; Subramaniam, K. Investigation of Alloy Composition and Sintering Parameters on the Corrosion Resistance and Microhardness of 316L Stainless Steel Alloy. *Adances Manuf. II* **2019**, *4*, 532–541.
2. Liu, X.; Xu, P.; Yao, L.; Li, X.; Pang, C.; Yang, L.; Liang, Y. Nb reinforced Fe-Mn-Si shape memory alloy composite coating fabricated by laser cladding on 304 stainless steel surface. *J. Mech. Sci. Technol.* **2022**, *36*, 5027–5033. [CrossRef]
3. Kenedy, G.R.; Lin, Y.-J.; Cheng, W.-C. Evidence of Martensitic Transformation in Fe-Mn-Al Steel Similar to Maraging Steel. *Metall. Mater. Trans. A* **2021**, *52*, 26–33. [CrossRef]
4. Wan, P.; Yu, H.; Li, F.; Gao, P.; Zhang, L.; Zhao, Z. Hot Deformation Behaviors and Process Parameters Optimization of Low-Density High-Strength Fe–Mn–Al–C Alloy Steel. *Met. Mater. Int.* **2022**, *28*, 2498–2512. [CrossRef]
5. Hou, Z.; Gu, W.; Li, T.; Wang, Z.; Li, L.; Yu, X.; Zhang, Y. A calibration-free model for laser-induced breakdown spectroscopy using non-gated detectors. *Front. Phys.* **2022**, *17*, 62503. [CrossRef]

6. Matsumoto, A.; Sakka, T. A Review of Underwater Laser-induced Breakdown Spectroscopy of Submerged Solids. *Anal. Sci.* **2021**, *37*, 1061–1072. [CrossRef] [PubMed]
7. Li, X.Y.; Liu, K.; Zhou, Z.; Zhang, W. Laser-Induced Breakdown Spectroscopy and Its Application. *Chin. J. Lasers* **2022**, *49*, 146–177.
8. Guo, L.-B.; Zhang, D.; Sun, L.-X.; Yao, S.-C.; Zhang, L.; Wang, Z.-Z.; Wang, Q.-Q.; Ding, H.-B.; Lu, Y.; Hou, Z.-Y. Development in the application of laser-induced breakdown spectroscopy in recent years: A review. *Front. Phys.* **2021**, *16*, 22500. [CrossRef]
9. Khan, Z.H.; Ullah, M.H.; Rahman, B.; Talukder, A.I.; Wahadoszamen, M.; Abedin, K.M.; Haider, A.F.M.Y. Evaluation of the prediction precision capability of partial least squares regression approach for analysis of high alloy steel by laser induced breakdown spectroscopy. *Spectrochimica Acta Part B: At. Spectrosc.* **2015**, *108*, 8–14.
10. Fiodor, S.; Francesco, C.G.F.; Francesconi, M.; Marsili; Cristoforetti, P.; Legnaioli, G.; Palleschi, S.; Tognoni, V. Fast analysis of complex metallic alloys by double-pulse time-integrated laser-induced breakdown spectroscopy. *Spectrochim. Acta Part B At. Spectrosc.* **2009**, *64*, 1068–1072.
11. Li, J.J.; Chen, F.; Zhang, S.; Wang, W.; Tang, Y.; Chu, Y.; Yao, J.; Guo, L. Identification of Graves' ophthalmology by laser-induced breakdown spectroscopy combined with machine learning method. *Front. Optoelectron.* **2021**, *14*, 321–328. [CrossRef] [PubMed]
12. Raja, H.; Akram, M.U.; Shaukat, A.; Khan, S.A.; Alghamdi, N.S.; Khawaja, S.G.; Nazir, N. Correction to: Extraction of Retinal Layers Through Convolution Neural Network (CNN) in an OCT Image for Glaucoma Diagnosis. *J. Digit. Imaging* **2021**, *34*, 1072. [CrossRef] [PubMed]
13. Sun, P.; Hao, X.; Hao, W.; Pan, B.; Yang, Y.; Liu, Y.; Tian, Y.; Jin, H. Laser-Induced Breakdown Spectral Separation Method for Bauxite Based on Convolutional Neural Network. *J. Appl. Spectrosc.* **2022**, *89*, 944–949. [CrossRef]
14. Pengfei, Z.; Ting, Z.; Daohua, X.; Li, Z. Quantitative analysis research of ChemCam-LIBS spectral data of Curiosity rover. *Infrared Laser Eng.* **2022**, *51*, 323–332.
15. Zhao, Y.; Guindo, M.L.; Xu, X.; Sun, M.; Peng, J.; Liu, F.; He, Y. Deep learning associated with laser-induced breakdown spectroscopy (LIBS) for the prediction of lead in soil. *Appl. Spectrosc.* **2019**, *73*, 565–573. [CrossRef] [PubMed]
16. Xu, X.; Du, C.; Ma, F.; Shen, Y.; Wu, K.; Liang, D.; Zhou, J. Detection of soil organic matter from laser-induced breakdown spectroscopy (LIBS) and mid-infrared spectroscopy (FTIR-ATR) coupled with multivariate techniques. *Geoderma* **2019**, *355*, 113905. [CrossRef]
17. Xing, P.; Dong, J.; Yu, P.; Zheng, H.; Liu, X.; Hu, S.; Zhu, Z. Quantitative analysis of lithium in brine by laser-induced breakdown spectroscopy based on convolutional neural network. *Anal. Chim. Acta* **2021**, *1178*, 338799. [CrossRef] [PubMed]